Petroleum Science 23 (2026) 1416–1427

Contents lists available at ScienceDirect

Petroleum Science

journal homepage: www.keaipublishing.com/en/journals/petroleum-science

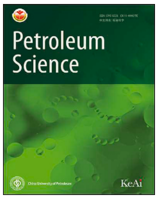

Original Paper

Experimental study of imbibition depth and oil migration mechanism of a magnetic nanofluid for low-permeability reservoir oil recovery improvement

Zhen-Feng Ma [a,b], Ming-Wei Zhao [a,b,*], Xiang-Yu Wang [c], Kai-Wen Liu [a,b], Yu-Xin Xie [a,b], Yi-Zheng Zhang [a,b], Zhong-Zheng Xu [a,b], Cai-Li Dai [a,b,**]

[a] State Key Laboratory of Deep Oil and Gas, China University of Petroleum (East China), Qingdao, 266580, Shandong, China
[b] Key Laboratory of Unconventional Oil & Gas Development, China University of Petroleum (East China), Ministry of Education, Qingdao, 266580, Shandong, China
[c] Sinopec Research Institute of Petroleum Engineering, Shale Oil Production Research Institute, Dongying, 257000, Shandong, China

ARTICLE INFO

Article history:
Received 22 March 2025
Received in revised form
13 November 2025
Accepted 13 November 2025
Available online 18 November 2025

Edited by Yan-Hua Sun

Keywords:
Magnetic nanofluid
Recyclable and reusable
Imbibition depth
Oil migration mechanism

ABSTRACT

Nanofluids are considered promising agents for enhanced oil recovery in low-permeability reservoirs, but their application is often restricted by poor thermal and saline resistance and high costs. Moreover, limited studies have addressed the imbibition depth and oil migration processes during nanofluid imbibition in low-permeability reservoirs. In this work, a magnetic core–shell structured nanoparticle Fe_3O_4–TiO_2 was synthesized using inexpensive Fe_3O_4 nanoparticles and tetrabutyl titanate. The synthesized nanoparticles exhibited excellent thermal and saline resistance as well as recyclability. Their structure and functional properties were characterized. The nuclear magnetic resonance technology was applied to investigate the imbibition depth and the oil migration process during magnetic nanofluid imbibition. Results showed that the magnetic nanofluid possessed interfacial activity, wettability alteration capability, and strong thermal and saline resistance. At 80 °C, the imbibition recovery of magnetic nanofluid reached 32.19%, 3.59% higher than that of SiO_2 nanofluid. The recycle rate of magnetic nanofluid was 81.31%, effectively reducing operational costs. The final imbibition depth of magnetic nanofluid reached 18.82 mm, with an average imbibition rate of 3.14 mm/d, which is 21.97% higher than that of the SiO_2 nanofluid and 39.10% higher than that of the simulated formation water. The imbibition process of magnetic nanofluid was dominated by capillary forces, with oil in micropores displaced into macropores. We expect that this study can contribute to the effective development of low-permeability reservoirs and provide theoretical guidance for field applications.

1. Introduction

In recent years, unconventional reservoirs, particularly low-permeability reservoirs, have demonstrated significant exploitation potential (Kang et al., 2022; Mahdaviara et al., 2022; Xie et al., 2022). However, due to the small pore throat sizes, poor permeability, and high heterogeneity of low-permeability reservoirs, crude oil extraction faces considerable challenges (Chen et al., 2022; Wang et al., 2023b). Imbibition refers to the process in which the wetting phase displaces the non-wetting phase under the influence of capillary forces within a porous medium (Liu et al., 2023; Xie et al., 2024). Depending on the experimental method, imbibition can be classified into static imbibition (Zhao et al., 2023) and dynamic imbibition (Wang et al., 2023a). Static imbibition occurs when the external fluid remains stationary, while dynamic imbibition takes place when the external fluid is flowing. Nanomaterials, with their small particle size and large specific surface area, can penetrate porous media and adsorb effectively at interfaces, thereby improving interfacial properties, which has

---

* Corresponding author.
** Corresponding author.
E-mail addresses: zhaomingwei@upc.edu.cn (M.-W. Zhao), daicl@upc.edu.cn (C.-L. Dai).
Peer review under the responsibility of China University of Petroleum (Beijing).

https://doi.org/10.1016/j.petsci.2025.11.026

attracted significant attention (Tavakkoli et al., 2022; Tohidi et al., 2022; Wu et al., 2024). Numerous studies have confirmed their effectiveness in accelerating the spontaneous imbibition process (Cao et al., 2024; Zhao et al., 2024).

Nanomaterials commonly used to enhance oil recovery face the issue of high operational costs. As a result, some researchers have begun investigating Fe_3O_4 nanoparticles, which can be recycled using magnetic fields or magnets, thus reducing operational costs. Paryoto et al. (2023) prepared a magnetic nanofluid using Fe_3O_4 nanoparticles and surfactants, achieving a total oil recovery of 76.50% of original oil in place (OOIP). Pereira et al. (2020) developed a functionalized Fe_3O_4-based magnetic nanofluid, with a recovery exceeding 60% in oil displacement experiment. They found that Fe_3O_4 nanoparticles could selectively remove smaller and more disordered asphaltene molecules. Surface modification of Fe_3O_4 nanoparticles has been a common strategy in previous studies to effectively overcome their poor dispersion stability and susceptibility to oxidation (Li et al., 2022; Liu et al., 2022). Some researchers have proposed the idea of preparing magnetic core–-shell structured nanoparticles, which involve coating Fe_3O_4 nanoparticles with other materials. Betancur et al. (2019) synthesized a magnetic iron core–carbon shell nanoparticle *via* a one-pot hydrothermal method and carbonization at 900 °C. After the oil displacement experiment, the recycle rate reached 98% using an external magnetic field. TiO_2, with its abundant hydroxyl groups, exhibits good hydrophilicity and dispersion stability (Caselli et al., 2024; Li et al., 2025). When used to modify Fe_3O_4 nanoparticles, TiO_2 significantly improves their dispersion in aqueous solutions (Li et al., 2021). Additionally, TiO_2 has a larger specific surface area, providing more active sites for reactions, making it a highly promising modification material for Fe_3O_4 nanoparticles.

Nuclear magnetic resonance technology, due to its low sample requirements, non-destructive analysis capabilities, large measurement scale and high precision, has attracted increasing attention from researchers. Gholinezhad et al. (2022) utilized nuclear magnetic resonance technology to study the one-dimensional imaging and relaxation time measurements of SiO_2 nanofluids. The results indicated that the presence of SiO_2 nanoparticles increased the imaging signal intensity and affected the relaxation time by shifting the curve toward faster time. Zhang et al. (2022) used nuclear magnetic resonance technology to monitor the distribution of oil in rock pores during the imbibition process with nanofluids. The results showed that medium pores were the dominant pore type in the rock, contributing the most to the imbibition recovery. Although nuclear magnetic resonance technology is well-developed, there is limited research on the imbibition depth and the oil migration process during nanofluid imbibition in low-permeability reservoirs using nuclear magnetic resonance technology. Therefore, more in-depth research is necessary to evaluate the potential of nanofluids for enhancing oil recovery through imbibition and their application prospects at the field scale.

In this work, a magnetic core–shell structured nanoparticle, Fe_3O_4–TiO_2, with excellent dispersion stability and recyclability, was synthesized *via* the sol-gel method and subsequently characterized. The dispersion stability, interfacial activity, wettability alteration capability and spontaneous imbibition performance of the magnetic nanofluid were systematically investigated. Finally, nuclear magnetic resonance technology was employed to explore the imbibition depth and the oil migration process during magnetic nanofluid imbibition, providing theoretical insights and technical support for the efficient development of low-permeability reservoirs.

2. Experimental method

2.1. Materials

In this work, Fe_3O_4 nanoparticles (99.5 wt%), tetrabutyl titanate (TBT, AR) and ammonia (28.0 wt%) were procured from Shanghai Macklin Biochemical Co., Ltd. Ethanol (AR), acetonitrile (99.8 wt%) and deuterium oxide (99.9 wt%) were sourced from Shanghai Aladdin Biochemical Technology Co., Ltd. Petroleum ether (AR) was acquired from Tianjin Fuyu Fine Chemical Co., Ltd. Commercially available SiO_2 nanofluid (SC-101, 0.1 wt%) was obtained from Shandong Yinfeng Nano New Material Co., Ltd. All chemicals were used as received without further purification. Deionized water and simulated formation water (3 wt% NaCl + 0.05 wt% $CaCl_2$) were prepared in the laboratory. Crude oil was obtained from the Shengli Oilfield. The experimental oil phase was simulated oil, prepared by mixing crude oil and kerosene in a mass ratio of 1:3, with a density of 0.85 g/cm^3. The artificial sandstone core samples, measuring 10 cm in length and 2.5 cm in diameter, were procured from Haian Oil Scientific Research Instruments Co., Ltd.

2.2. Synthesis of the Fe_3O_4–TiO_2 nanoparticles

The synthesis of Fe_3O_4–TiO_2 was based on the sol-gel method reported in the literature (Li et al., 2021). TBT was used as the titanium source to coat TiO_2 onto the surface of Fe_3O_4 nanoparticles *via* this method, with the synthesis steps and principles illustrated in Fig. 1. Initially, 2 g of Fe_3O_4 nanoparticles, 80 g of ethanol and 40 g of acetonitrile were sequentially added to a three-necked flask and sonicated until the Fe_3O_4 nanoparticles were stably dispersed. Subsequently, under continuous stirring, 4 g of TBT and 4 g of ammonia were slowly added dropwise. After the addition was complete, stirring was continued for an additional 5 h. The reaction product was then left to stand at room temperature for 24 h, followed by magnetic separation, washing three times with ultrapure water, and vacuum drying at 50 °C for 12 h.

The sol-gel method primarily involves hydrolysis, dehydration, and alcoholysis polymerization reactions. During hydrolysis, alkoxide groups are replaced by nucleophilic attack from oxygen atoms in water molecules, releasing alcohol and forming hydroxylated titanium. The hydroxylated titanium undergoes dehydration polymerization to form Ti–O–Ti bonds and water, while alcoholysis polymerization results in the formation of Ti–O–Ti bonds and alcohol (Behzadnia et al., 2014).

2.3. Characterization of the Fe_3O_4–TiO_2 nanoparticles

The dispersion, microstructure, and shell thickness of Fe_3O_4–TiO_2 were characterized using a multi-angle particle size and high-sensitivity zeta potential analyzer (Brookhaven, Omni), as well as a transmission electron microscope (Thermo Fisher, Tecnai G2 20). The chemical structure and composition of the surfaces of Fe_3O_4 and Fe_3O_4–TiO_2 were analyzed using a Fourier transform infrared spectrometer (Thermo Fisher, Nicolet 6700). To further analyze the surface functional groups of Fe_3O_4–TiO_2, an X-ray photoelectron spectrometer (Thermo Fisher, K-Alpha) was employed. The magnetic properties of Fe_3O_4 and Fe_3O_4–TiO_2 were characterized using a vibrating sample magnetometer (Lake Shore, 7404).

2.4. Preparation and stability of the magnetic nanofluid

The magnetic nanofluid was prepared by adding 0.1 wt% Fe_3O_4–TiO_2 to ultrapure water and ultrasonically dispersing the

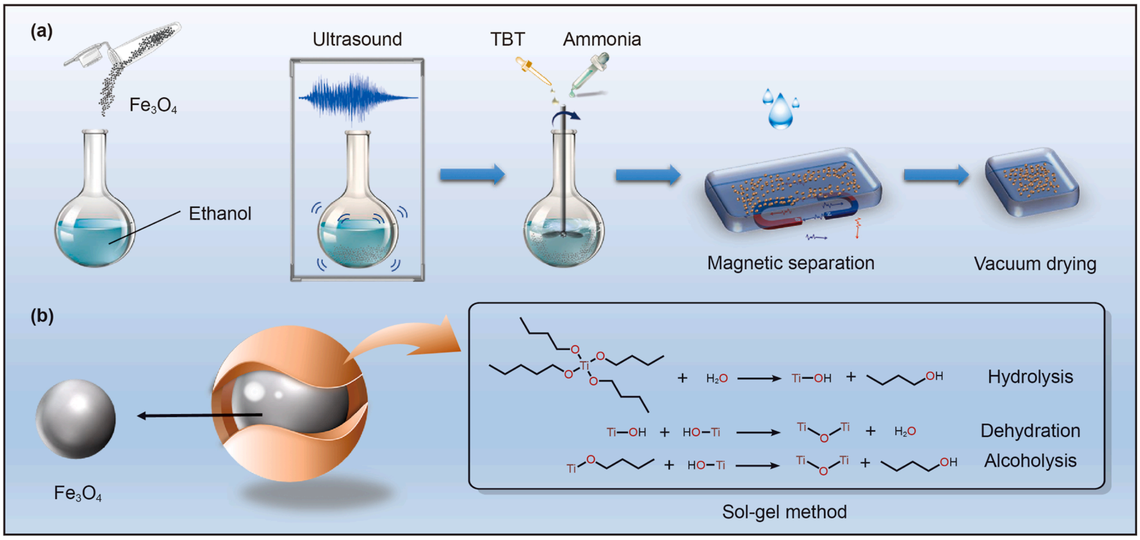

Fig. 1. Synthesis steps and principles of Fe_3O_4–TiO_2.

mixture at room temperature for 10 min using an ultrasonic dispersion machine (Xinzhi, JY92-IIN). Based on the conditions of a well in the Shengli Oilfield, 3 wt% NaCl and 0.05 wt% $CaCl_2$ were added to the magnetic nanofluid, which was then placed in an oven at 120 °C. The particle size and zeta potential of the magnetic nanofluid were periodically measured to evaluate its stability.

2.5. Interfacial tension and contact angle measurements

The interfacial tension between various systems and the simulated oil was measured using a full-range rotational interfacial tensiometer (Shengwei, TX-500C) by employing the spinning drop method (Esfandiarian et al., 2022; Song et al., 2025). First, the quartz sample tube was cleaned with petroleum ether to remove residual oil, followed by ethanol to remove the petroleum ether. The sample tube was then rinsed three times with the test liquid. Once the instrument temperature reached 80 °C, the sample tube containing the test liquid and a simulated oil drop was placed into the instrument, and the rotational speed was set to 8000 rpm. After the oil drop shape was stable, a snapshot of the oil drop shape was taken, and the interfacial tension was calculated.

The effect of the magnetic nanofluid on the contact angle was studied using a contact angle meter (Zhongchen, JC2000D). To obtain oil-wet surfaces, the dried core slices were saturated with simulated oil and then aged at 80 °C for two weeks. The oil-wet core slice was then mounted on a holder inside a quartz container, and a drop of water was placed on the surface to capture an initial snapshot of the droplet profile. Afterward, the core slice was immersed in the magnetic nanofluid for 24 h, removed, and another water droplet was placed on its surface for a second snapshot. The wettability alteration capability of the magnetic nanofluid was evaluated by comparing the initial and final contact angles.

2.6. Spontaneous imbibition performance

To investigate the spontaneous imbibition performance of the magnetic nanofluid, a static spontaneous imbibition apparatus was used to compare and evaluate the imbibition recovery of the magnetic nanofluid, SiO_2 nanofluid and simulated formation water. The detailed experimental procedure is as follows:

(1) The core samples were cut into blocks of approximately 2.5 cm in length, and the end faces were polished with sandpaper. The core samples were then repeatedly washed with ultrapure water, followed by ultrasonic cleaning for 1 h to remove surface impurities. Afterward, the core samples were dried in a constant-temperature oven at 110 °C for 24 h. After cooling, the length, diameter, mass, permeability and porosity of core samples were measured, with the results shown in Table 1.
(2) The core samples and simulated oil were placed in a vacuum high-pressure saturation apparatus. Both the core samples and the simulated oil were simultaneously vacuumed for 12 h. Then, the valve between them was opened, allowing the pressure difference to saturate the core samples with simulated oil. Vacuuming was continued for another 12 h. After saturation, the core samples and simulated oil were placed in an oven at 80 °C for 48 h for aging.
(3) The mass of the core samples saturated with simulated oil was measured, and then the core samples and solutions were sequentially placed in a static spontaneous imbibition apparatus. The experiment was conducted at 80 °C, and the volume of simulated oil in the glass tube at the top of the apparatus was recorded at regular intervals. The imbibition recovery can be calculated as follows:

$$E_R = \frac{V_0 \rho_0}{m_1 - m_0} \times 100\% \tag{1}$$

where E_R represents the oil recovery during spontaneous imbibition; V_0 is the volume of the recovered oil phase, mL; ρ_0 denotes the density of the simulated oil, g/cm^3; m_0 and m_1 represent the mass of the core samples before and after saturation, g.

Table 1
Specific core sample parameters of spontaneous imbibition test.

Number	Length, cm	Diameter, cm	Permeability, mD	Porosity, %
1	2.30	2.52	2.16	18.69
2	2.39	2.51	2.28	16.44
3	2.36	2.52	2.12	18.01

2.7. Recyclability of the magnetic nanofluid

Based on the aforementioned spontaneous imbibition experiments, the recyclability of the magnetic nanofluid was evaluated using a magnet. The magnet was placed into the produced fluid from the magnetic nanofluid spontaneous imbibition experiment. After standing for 30 min, the magnet was slowly removed from the produced fluid and dried. The mass of the adsorbed magnetic nanoparticles was measured. The recycle rate of the magnetic nanofluid was then calculated by comparing this mass with the mass of magnetic nanoparticles used in the preparation of the nanofluid prior to the imbibition experiment. To ensure the accuracy of the results, the recycle rate was tested three times and taken the average value. The recycled magnetic nanoparticles were re-dispersed to prepare magnetic nanofluid, which was then used in a subsequent spontaneous imbibition experiment to evaluate the recyclability of the magnetic nanofluid.

2.8. Nuclear magnetic resonance measurement

2.8.1. Imbibition depth

To investigate the spontaneous imbibition depth of magnetic nanofluid, a simulated core was placed on one side of the core sample, and a fluorinated ethylene propylene transparent heat-shrink tube (FEPT) was tightly wrapped around their surface using a heat gun (Niumag, ZY-866), leaving only one side exposed for unilateral imbibition, as shown in Fig. 2. The diameters of the simulated core and the experimental core sample were identical, with the simulated core used to seal one side of the experimental core sample. Both the simulated core and the FEPT are primarily composed of polytetrafluoroethylene, a non-paramagnetic substance that minimally interferes with the magnetic field (Yan et al., 2024). Before wrapping the FEPT around the surface, the core sample was saturated with simulated oil and aged, with specific parameters provided in Table 2.

During the experiment, magnetic nanofluid, SiO_2 nanofluid and simulated formation water were prepared using deuterium oxide. Deuterium oxide is a substance that does not produce nuclear magnetic resonance signals in a magnetic field and has the same physicochemical properties as regular water (Liu et al., 2024). Thus, interference from water signals is eliminated, allowing the frequency-encoded Q-HSE sequence of a core NMR and MRI analyzer (Niumag, MacroMR12-150H-I) to detect the nuclear magnetic resonance signals of a specific profile within the core sample during the unilateral imbibition process, which are then converted into one-dimensional profile signals. The signals were scanned every 24 h, and the water saturation along the imbibition direction can be calculated as follows:

$$S_{wx} = \frac{Q_{xi} - Q_{xt}}{Q_{xi} - Q_b} \tag{2}$$

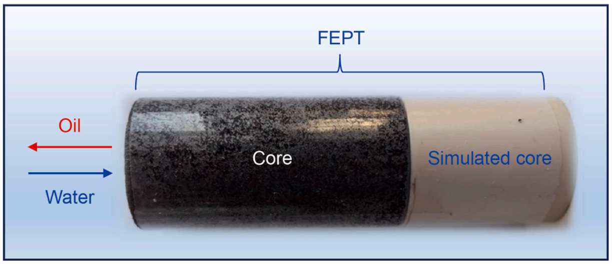

Fig. 2. Photograph of the unilateral imbibition experiment.

Table 2
Specific core sample parameters of unilateral imbibition experiment.

Number	Length, cm	Diameter, cm	Permeability, mD	Porosity, %
4	2.91	2.51	2.28	16.93
5	2.96	2.51	2.67	16.23
6	2.84	2.50	2.36	16.05

where S_{wx} represents the water saturation at a distance of x from the imbibition surface; Q_{xi} is the initial signal amplitude at position x; Q_{xt} denotes the signal amplitude at time t at position x; and Q_b represents the baseline signal amplitude at position x.

2.8.2. Imaging and T_2 spectra

To investigate the oil migration process in core samples during magnetic nanofluid imbibition, nuclear magnetic resonance imaging and T_2 spectrum analysis were conducted during spontaneous imbibition experiments. The specific parameters of the core samples used in the experiments are listed in Table 3. Both the magnetic nanofluid and the simulated formation water were prepared using deuterium oxide. Measurements were taken every 48 h.

3. Results and discussion

3.1. Characterization of Fe_3O_4 and Fe_3O_4–TiO_2 nanoparticles

The particle sizes of Fe_3O_4 and Fe_3O_4–TiO_2 were measured by dynamic light scattering, with the experimental results shown in Fig. 3(a). The particle size of Fe_3O_4 is 15.96 nm, while that of Fe_3O_4–TiO_2 is 17.72 nm, suggesting that the thickness of the titanium shell is approximately 2 nm. Additionally, the zeta potential of the magnetic nanofluid is −44.58 mV. According to previous studies (Dembek et al., 2022; Kosmulski and Mączka, 2022), nanofluids are considered stable when the absolute value of zeta potential exceeds 30 mV. Therefore, the magnetic nanofluid exhibits good dispersion stability.

The microstructures of Fe_3O_4 and Fe_3O_4–TiO_2 are shown in Fig. 3(b) and (c), respectively. Both Fe_3O_4 and Fe_3O_4–TiO_2 exhibit quasi-spherical morphology with small particle sizes, primarily ranging from 10 to 20 nm, consistent with the particle size distribution measured by dynamic light scattering. Compared to Fe_3O_4, the dispersion of Fe_3O_4–TiO_2 is significantly improved, with no obvious large-scale aggregation and a more uniform particle size distribution. This indicates that the TiO_2 coating on the Fe_3O_4 surface effectively addresses the poor dispersion of Fe_3O_4.

The FT-IR spectra of Fe_3O_4 and Fe_3O_4–TiO_2 within the range of 4000–500 cm^{-1} are presented in Fig. 3(d). The O–H stretching vibration peaks are observed at 3409 cm^{-1} for Fe_3O_4 and 3208 cm^{-1} for Fe_3O_4–TiO_2. The C=O stretching vibration peaks appear at 1631 and 1639 cm^{-1}. Fe–O stretching vibration peaks are detected at 581 and 568 cm^{-1}. Additionally, a Ti–O stretching vibration peak at 1406 cm^{-1} for Fe_3O_4–TiO_2 indicates the successful coating of TiO_2 on the surface of Fe_3O_4 nanoparticles, confirming the successful synthesis of Fe_3O_4–TiO_2. The results demonstrate that the surface of Fe_3O_4–TiO_2 contains carbonyl, hydroxyl, and titanium-containing functional groups with abundant active sites.

Table 3
Specific core sample parameters of imaging and T_2 spectra experiment.

Number	Length, cm	Diameter, cm	Permeability, mD	Porosity, %
7	2.28	2.50	2.46	14.73
8	2.32	2.50	2.17	14.78

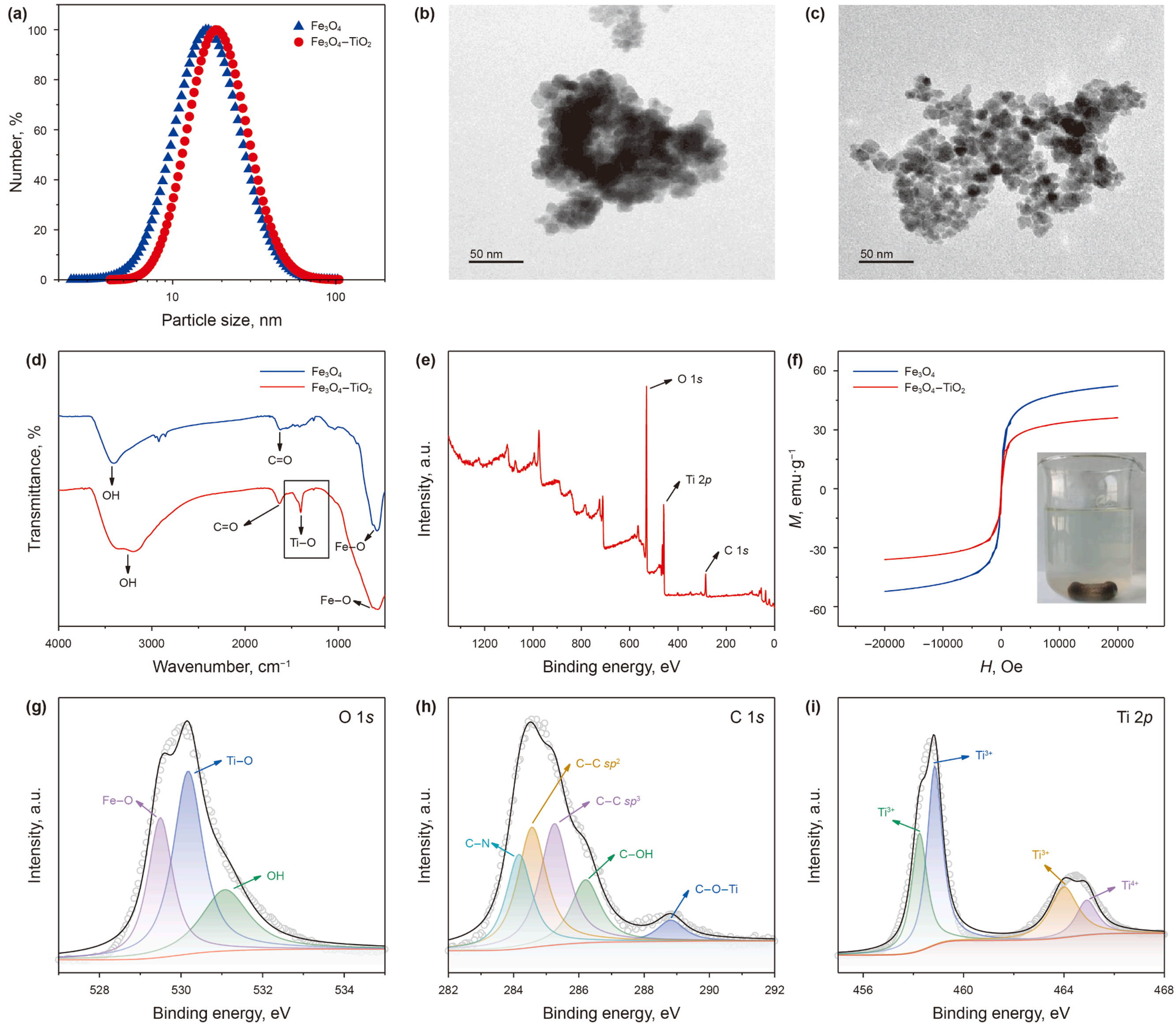

Fig. 3. (**a**) Particle size distribution of Fe_3O_4 and Fe_3O_4–TiO_2. TEM images of Fe_3O_4 (**b**) and Fe_3O_4–TiO_2 (**c**). (**d**) FT-IR spectra of Fe_3O_4 and Fe_3O_4–TiO_2. (**e**) XPS spectra of Fe_3O_4–TiO_2. (**f**) Magnetic hysteresis loop of Fe_3O_4 and Fe_3O_4–TiO_2. O 1*s* (**g**), C 1*s* (**h**) and Ti 2*p* (**i**) spectra of Fe_3O_4–TiO_2.

Moreover, the presence of numerous hydrophilic functional groups on the surface of Fe_3O_4–TiO_2 ensures its good dispersibility and stability in aqueous solutions.

The XPS results of Fe_3O_4–TiO_2 are shown in Fig. 3(e). The peak at 530 eV represents the O 1*s* binding energy of the O element on the surface of Fe_3O_4–TiO_2, the peak at 459 eV corresponds to the Ti 2*p* binding energy of the Ti element, and the peak at 285 eV corresponds to the C 1*s* binding energy of the C element. These results indicate that the surface of Fe_3O_4–TiO_2 is primarily composed of O, Ti and C elements.

The peak deconvolution of the XPS spectra for Fe_3O_4–TiO_2 provided the O 1*s*, C 1*s* and Ti 2*p* spectra. As shown in Fig. 3(g), the O 1*s* spectrum of Fe_3O_4–TiO_2 reveals three characteristic peaks corresponding to Fe–O (529.5 eV), Ti–O (530.2 eV) and OH (531.1 eV). In the C 1*s* spectrum (Fig. 3(h)), five characteristic peaks are observed, attributed to C—N (284.1 eV), C—C sp^2 (284.6 eV), C—C sp^3 (285.3 eV), C—OH (286.2 eV) and C—O—Ti (288.8 eV). The Ti 2*p* spectrum (Fig. 3(i)) exhibits four characteristic peaks, corresponding to Ti^{3+} (458.3 eV), Ti^{3+} (458.9 eV), Ti^{3+} (464.9 eV), and Ti^{4+} (464.9 eV). The XPS analysis results are consistent with the FT-IR spectrum findings, confirming the presence of a variety of functional groups and abundant active sites on the surface of Fe_3O_4–TiO_2. This indicates that the method used for preparing Fe_3O_4–TiO_2 is effective and reliable.

Vibrating sample magnetometer is used to assess the magnetic strength by observing the magnetic moment (*M*), which indicates how the material reacts to an applied alternating magnetic field (*H*) (Rouhani et al., 2022; Zarandona et al., 2023). The data obtained from these magnetic field variations form a loop known as the magnetic hysteresis loop (Li et al., 2023; Nguyen et al., 2024). The magnetic hysteresis loop for Fe_3O_4 and Fe_3O_4–TiO_2 are shown in Fig. 3(f). Both of them exhibit S-shaped curves with no hysteresis, remanence or coercivity, indicating that two nanoparticles are superparamagnetic. After coating Fe_3O_4 with TiO_2, the saturation magnetic intensity decreased from 52.38 to 36.09 emu·g^{-1}, which still remains sufficient for the rapid magnetic separation.

When a magnet was placed into the Fe_3O_4–TiO_2 solution, a satisfactory magnetic response was observed within 10 min, confirming that Fe_3O_4–TiO_2 can be efficiently and quickly recycled.

3.2. Stability of the magnetic nanofluid

Dispersion stability is a prerequisite for the application of nanofluids. Fig. 4 shows the variation trends of particle size and absolute value of zeta potential of the magnetic nanofluid over time under 120 °C and reservoir salinity conditions. It can be observed that, during the experimental period, the particle size of the magnetic nanofluid remained stable, while the absolute value of zeta potential slightly decreased with time, remaining at 37.97 mV after 192 h. Therefre, the magnetic nanofluid exhibits good dispersion stability as well as temperature and salinity resistance, making it suitable for further research.

3.3. Interfacial tension and contact angle

The interfacial tension between simulated oil droplets and magnetic nanofluids of different concentrations is shown in Fig. 5(a). As the concentration of the magnetic nanofluid increases, the interfacial tension decreases. The interfacial tension of simulated oil droplets in pure water is 21.58 mN/m, while in 0.1 wt% magnetic nanofluid, it is reduced to 6.63 mN/m, a decrease of 69.28%. This reduction is primarily attributed to the adsorption of Fe_3O_4–TiO_2 at the oil–water interface. The surface of these nanoparticles contains various functional groups, such as carbonyl, hydroxyl, and titanium-containing groups, which interact with both the oil and water phases. By adsorbing at the interface, the nanoparticles reduce interfacial free energy, alter the interfacial molecular arrangement, and consequently decrease the interfacial tension.

The contact angle morphology of water droplets on the core sample surface before and after treatment with magnetic nanofluid is shown in Fig. 5(b) and (c). The magnetic nanofluid can change the wettability of the core sample surface from oil-wet (contact angle greater than 90°) to water-wet (contact angle less than 90°). Before treatment with the magnetic nanofluid, the contact angle of the water droplet was 100°. While after treatment, it decreased to 33°, showing a significant wettability alteration effect. After entering the reservoir, the magnetic nanoparticles adsorb onto the oleophilic rock surface and increase the hydrophilicity of the rock, facilitating the detachment of oil droplets. Additionally, once the rock surface wettability shifts from oil-wet to water-wet, the adhesion of crude oil on the formation surface during pore flowing is significantly reduced, which aids in the extraction of oil droplets (Elkhatib et al., 2024; Noruzi et al., 2024).

3.4. Spontaneous imbibition performance and recyclability

The spontaneous imbibition recovery curves for magnetic nanofluid, SiO_2 nanofluid, and simulated formation water are shown in Fig. 6(a). The recovery curves of the three systems exhibit similar trends, with a rapid increase during the initial phase. However, after 72 h of imbibition, the recovery increases at a slower pace and eventually stabilizes. Compared to the SiO_2 nanofluid and simulated formation water, the magnetic nanofluid demonstrates better oil recovery performance, not only increasing the final recovery, but also shortening the initiation time. The final oil recovery for the magnetic nanofluid is 32.19%, while for the SiO_2 nanofluid, the recovery is 28.60%, and for simulated formation water, it is only 6.81%. This improvement is attributed to the fact that magnetic nanoparticles can not only reduce interfacial tension, but also change the wettability of the core sample from oil-wet to water-wet, facilitating the detachment of oil droplets.

The recycle results of the magnetic nanofluid are shown in Table 4. The average recycle rate of the magnetic nanofluid in the spontaneous imbibition experiment is 81.31%, which is attributed to some of the magnetic nanoparticles entering the interior of the core sample. Overall, the majority of magnetic nanoparticles can be recycled and reused after the experiment, significantly reducing the operational costs.

The magnetic nanoparticles recycled using a magnet were reconstituted into a magnetic nanofluid, and the imbibition performance of the recycled nanofluid was evaluated. The experimental results are shown in Fig. 6(b). The final imbibition recovery for the magnetic nanofluid and the recycled magnetic nanofluid was 32.19% and 31.21%, respectively. This indicates that the performance of the recycled magnetic nanoparticles remains unaffected and they can be reused, demonstrating their high potential for practical applications.

3.5. Imbibition depth

The magnetic nanofluid, upon entering the fracture of the reservoir, undergoes imbibition with the crude oil in the near-

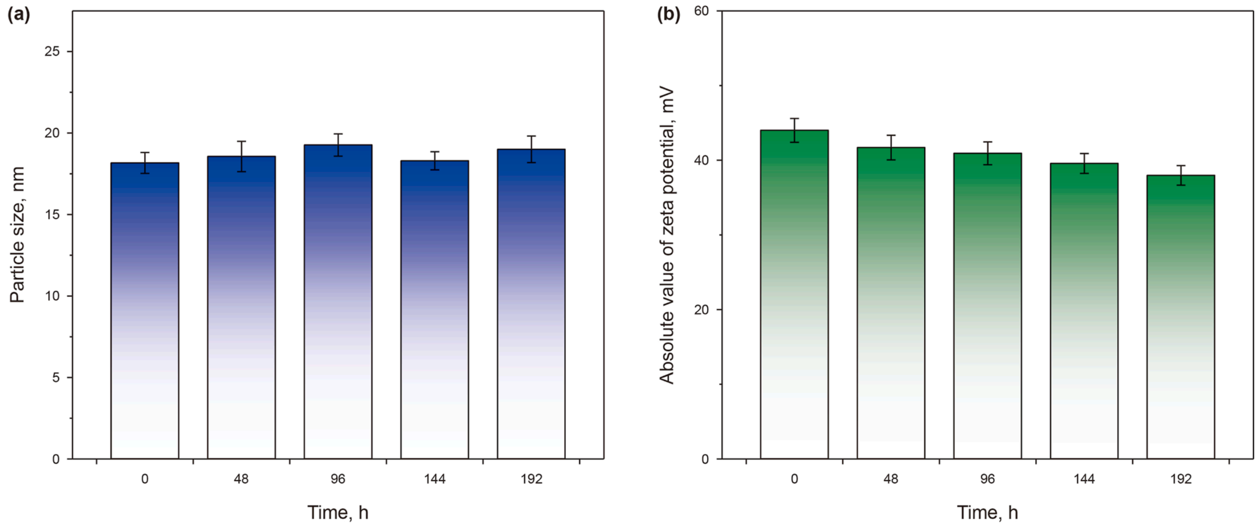

Fig. 4. The variation of particle size (**a**) and absolute value of zeta potential (**b**) of magnetic nanofluid over time under high temperature and high salinity conditions.

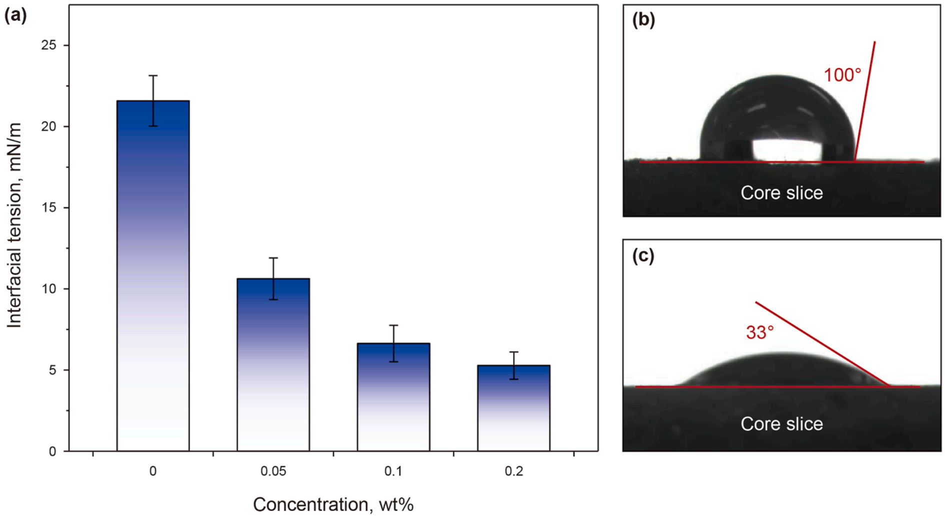

Fig. 5. (**a**) The interfacial tension between simulated oil and magnetic nanofluids of different concentrations. The static water contact angle on surface of the core sample before (**b**) and after (**c**) treatment with magnetic nanofluid.

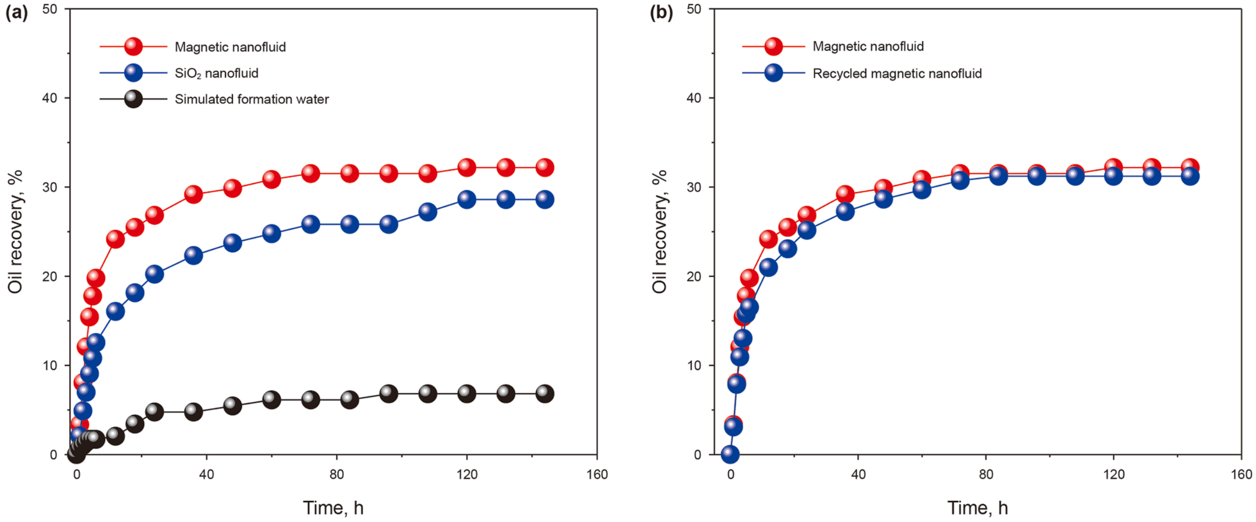

Fig. 6. (**a**) The imbibition recovery curves for different systems. (**b**) The imbibition recovery curves of the magnetic nanofluid before and after recycling.

Table 4
The results of the recycle experiments.

Experimental number	Initial mass, g	Recycle mass, g	Recycle rate, %	Average recycle rate, %
1	0.5032	0.4099	81.46	81.31
2	0.5016	0.4206	83.85	
3	0.5008	0.3937	78.61	

fracture matrix (Meng et al., 2024). It is crucial to determine the imbibition depth and effect. The nuclear magnetic resonance signals along the unilateral imbibition direction of the core sample for the magnetic nanofluid, SiO_2 nanofluid and simulated formation water are shown in Fig. 7(a)–(c), respectively. The curves are divided into three areas: effective signal, transition area, and noise signal (Yan et al., 2024). The intensity of the effective signal is significantly higher than the noise signal outside the core sample, indicating a high signal-to-noise ratio for this experimental method, and the results are reliable and valid. As the unilateral imbibition progresses, the effective signals near the imbibition surface of the core sample in all three experiments gradually weaken, indicating that the fluids displace the oil from the imbibition surface upon entering the core sample. Oil far from the imbibition surface is more difficult to displace. Compared with SiO_2 nanofluid and simulated formation water, the effective signal intensity of the magnetic nanofluid decreases more significantly, suggesting that the magnetic nanofluid not only penetrates deeper into the oleophilic core sample, but also enhances the efficiency of oil displacement in the penetrated region. Furthermore, this effect becomes more pronounced over time.

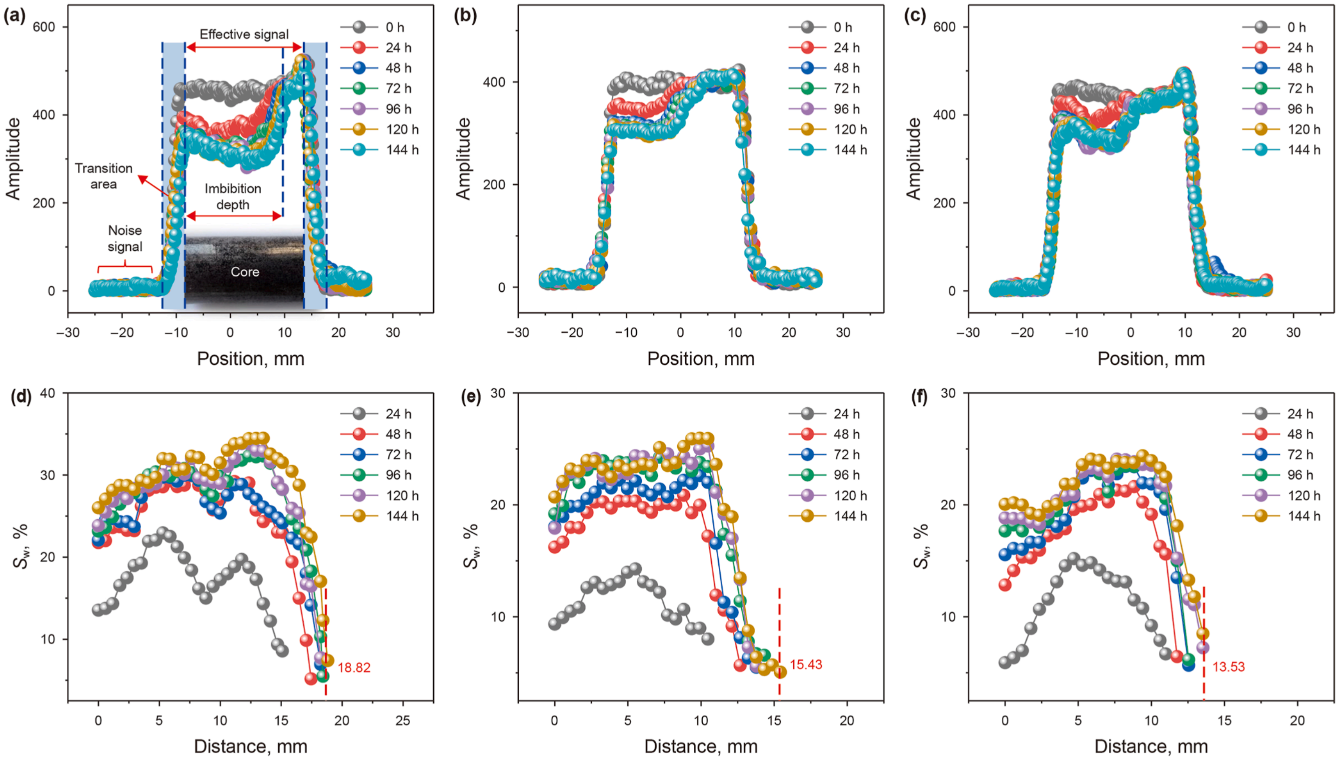

Fig. 7. The nuclear magnetic resonance spectra of the experimental core samples during unilateral imbibition in magnetic nanofluid (**a**), SiO_2 nanofluid (**b**), and simulated formation water (**c**). The water saturation distribution of the experimental core samples during unilateral imbibition in magnetic nanofluid (**d**), SiO_2 nanofluid (**e**) and simulated formation water (**f**).

To accurately describe the water saturation distribution within the core samples, the conversion of nuclear magnetic resonance signals to water saturation was based on the following three conversion criteria (Liu and Sheng, 2020): (1) The initial oil saturation of the core sample was assumed to be 100%, the magnetic nanofluid, SiO_2 nanofluid, and simulated formation water all displaced the simulated oil through reverse imbibition, and the increase in core sample water saturation was equal to the imbibition recovery. (2) At the core sample imbibition surface, the signal did not directly transition from the noise signal to the effective signal, and a transition area was observed. This was due to the volatilization of simulated oil near the imbibition surface or the non-perpendicular orientation of the core sample cross-section to the magnetic field. The initial imbibition surface was defined as the vertical plane corresponding to the highest point of the slanted line at the end. (3) Along the imbibition direction extending into the rock, the nuclear magnetic resonance signal was gradually weakened, and the imbibition effect was diminished. Due to the presence of noise signals, the value was typically below 50, while effective signals were generally above 200. Therefore, the final imbibition surface was chosen as the vertical interface corresponding to the first point where water saturation was below 5%.

Based on the above principles, the water saturation along the x-axis during unilateral imbibition experiments with magnetic nanofluid, SiO_2 nanofluid, and simulated formation water are presented in Fig. 7(d)–(f), respectively. As imbibition progresses, both the water saturation and imbibition depth increase, but the rate of increase gradually decreases with time until equilibrium is reached. The final imbibition depths of the core samples in magnetic nanofluid, SiO_2 nanofluid, and simulated formation water are 18.82, 15.43, and 13.53 mm, respectively. The imbibition depth of magnetic nanofluid is 21.97% and 39.10% greater than that of SiO_2 nanofluid and simulated formation water, respectively, with consistently higher water saturation across all positions. This enhancement can be attributed to the ability of the magnetic nanofluid to partially reduce interfacial tension, coupled with its strong wettability alteration capability, thereby improving oil displacement efficiency. Additionally, the change in core sample wettability alters the direction of capillary forces, facilitating further penetration of the magnetic nanofluid into the core sample (Valiei et al., 2022; Wang et al., 2023c). The imbibition depth is an important parameter for evaluating imbibition efficiency, which remains independent of rock size and can be applied to real field scale.

3.6. Nuclear magnetic resonance imaging and T_2 spectrum analysis

To visualize the distribution of simulated oil in the core samples during the imbibition process using magnetic nanofluid and simulated formation water, two-dimensional nuclear magnetic resonance images of core samples were obtained using imaging technology, as shown in Fig. 8. The green color represents the variation in simulated oil content within the core samples. In the initial images, the entire core sample appears bright green, indicating strong nuclear magnetic resonance signals and the core sample pores were fully filled with simulated oil. As the imbibition process progresses, the brightness of the green region in the core sample treated with magnetic nanofluid gradually decreases, suggesting that simulated oil was progressively displaced from the core sample pores. Additionally, the decrease in signal intensity is uniform, with no formation of distinct preferential flow channels, indicating that this is the result of spontaneous imbibition. As the imbibition time increases, the distribution of simulated oil in the core sample treated with simulated formation water shows little

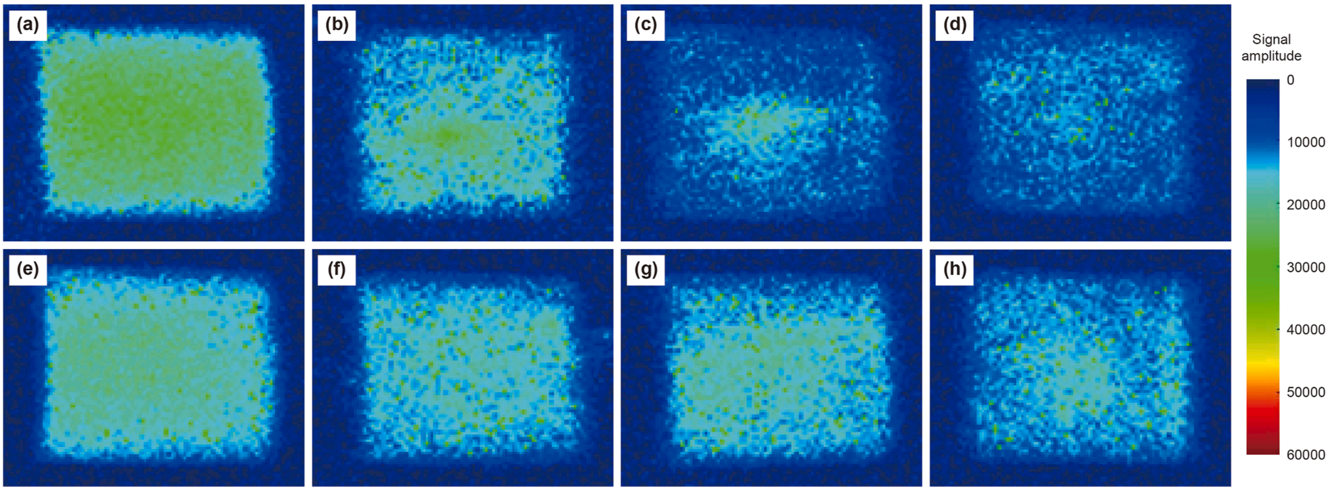

Fig. 8. Nuclear magnetic resonance images of the core sample in magnetic nanofluid at imbibition time of 0 h (initial state) (**a**), 48 h (**b**), 96 h (**c**) and 144 h (**d**). Nuclear magnetic resonance images of the core sample in simulated formation water at imbibition time of 0 h (initial state) (**e**), 48 h (**f**), 96 h (**g**) and 144 h (**h**).

change, with the signal intensity inside the core sample remaining relatively strong. Only the peripheral regions show some degree of reduction, indicating that the simulated oil did not migrate within the core sample pores.

Based on the method described in the literature (Wang et al., 2018), the conversion coefficient C in Eq. (3) can be determined using the T_2 spectra and mercury intrusion results. This allows for the identification of the corresponding relaxation time and pore diameter ranges for the micropores, mesopores, and macropores in experimental core samples.

$$d = CT_2 \tag{3}$$

where d represents the pore diameter, μm; C is the conversion coefficient, μm·ms^{-1}; and T_2 denotes the relaxation time, ms.

To determine the value of C, the core sample mercury intrusion curve and the initial T_2 spectrum were compared, as shown in Fig. 9. Five points corresponding to relaxation time and pore diameter were selected and the average conversion coefficient was calculated. The specific results are shown in Table 5, the average conversion coefficient for the experimental core sample was determined to be 1.78 μm·ms^{-1}, which allowed for the identification of the corresponding relaxation time and pore diameter ranges for micropores, mesopores, and macropores in the core sample. Pores with a diameter smaller than 1.39 μm and relaxation time smaller than 0.78 ms were classified as micropores, pores with diameters ranging from 1.39 to 62.10 μm and relaxation time from 0.78 to 34.89 ms as mesopores, and pores with diameters larger than 62.10 μm and relaxation time greater than 34.89 ms as macropores.

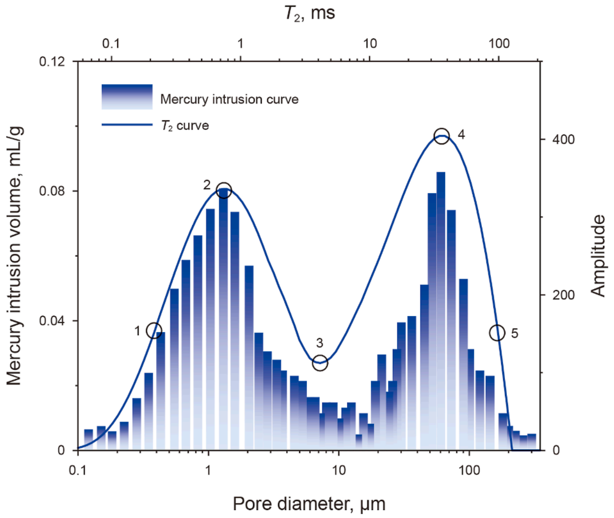

Fig. 9. The core sample mercury intrusion curve and the initial nuclear magnetic resonance T_2 spectrum.

The nuclear magnetic resonance T_2 spectra of the experimental core samples in magnetic nanofluid and simulated formation water at different imbibition time are shown in Fig. 10(a) and (d), respectively. The T_2 distribution exhibits a bimodal pattern. In the early stages of imbibition, the signal intensity of the T_2 spectrum in magnetic nanofluid decreases significantly, with varying degrees of mobilization in micropores, mesopores and macropores. After 96 h, the signal intensity remains almost unchanged, indicating that the volume of simulated oil within the experimental core sample no longer decreases. In the case of simulated formation water, the spectrum shows that the mobilization of simulated oil in the core sample pores is minimal, with only a small amount of oil being mobilized from mesopores and macropores, indicating that the effect of simulated formation water on core sample imbibition is limited.

To further investigate the mobilization of simulated oil in different pore types during various imbibition stages, the area under the curves for different pore sizes in Fig. 10(a) and (d) was calculated through integration. The mobilization of simulated oil in micropores, mesopores, and macropores at different imbibition stages is shown in Fig. 10(b) and (e).

In the early stage of imbibition with magnetic nanofluid, the mobilization of simulated oil in micropores and mesopores was

Table 5
Calculation of the average conversion coefficient.

Number	T_2, ms	d, μm	C, μm·ms^{-1}
1	0.21	0.43	2.05
2	0.71	1.31	1.85
3	4.15	7.24	1.74
4	34.89	60.68	1.74
5	96.59	144.68	1.50

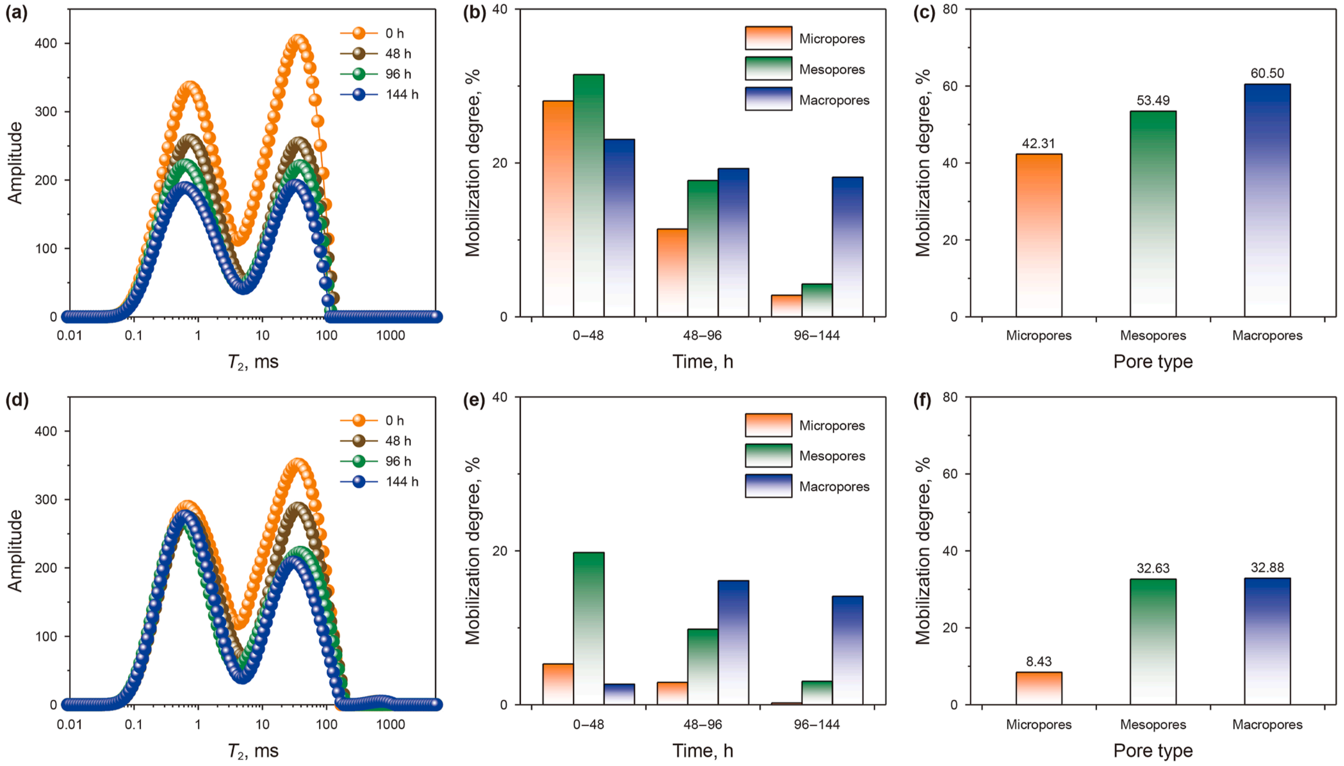

Fig. 10. The T_2 spectrum (**a**), pore mobilization behavior (**b**), and final pore mobilization degree (**c**) during the imbibition process of the experimental core sample with magnetic nanofluid. The T_2 spectrum (**d**), pore mobilization behavior (**e**), and final pore mobilization degree (**f**) during the imbibition process of the experimental core sample with simulated formation water.

higher than that in macropores. During the 0–48 h period, the mobilization in micropores, mesopores, and macropores was 28.08%, 31.49%, and 23.06%, respectively. This is because the smaller pore size results in higher capillary forces, as derived from the capillary force equation. Under constant interfacial tension and contact angle conditions, a smaller capillary radiu leads to greater capillary force. Consequently, the higher capillary force in micropores caused water to be absorbed, while macropores expel oil. As a result, magnetic nanofluid first enters micropores and mesopores to displace the simulated oil, which is then expelled into macropores.

In the middle stage of imbibition, the mobilization of simulated oil in mesopores and macropores was higher. During the 48–96 h period, the mobilization in micropores, mesopores, and macropores was 11.41%, 17.73%, and 19.28%, respectively. This is because micropores, with diameters less than 1.39 μm, have a more complex pore structure, and a greater proportion of non-accessible pores. In contrast, mesopores and macropores have relatively simpler structures, leading to higher mobilization in the later stages.

In the late stage of imbibition, large pores exhibited the highest mobilization of simulated oil. During the 96–144 h period, the mobilization of simulated oil in macropores was 18.16%, while in micropores and mesopores, it was 2.82% and 4.27%, respectively. At this stage, the mobilization of simulated oil in micropores and mesopores approached equilibrium, and magnetic nanofluid continued to enter macropores, further displacing simulated oil. As a result, the mobilization in macropores continued to increase.

In contrast, the mobilization of simulated oil by simulated formation water in micropores was very low, with only a small amount of oil being mobilized from mesopores and macropores.

The final mobilization degrees of different pore types with magnetic nanofluid and simulated formation water are shown in Fig. 10(c) and (f). In the magnetic nanofluid, the mobilization degrees of simulated oil in micropores, mesopores, and macropores were 42.31%, 53.49%, and 60.50%, respectively. In the simulated formation water, the mobilization degrees in mesopores and macropores were 32.63% and 32.88%, while the mobilization degree in micropores was only 8.43%. The comparison reveals that the addition of magnetic nanoparticles improved the simulated oil mobilization degree in all pore types, with the most significant effect observed in micropores. This is attributed to the excellent interfacial activity and wettability alteration capability of the magnetic nanoparticles, which allow them to penetrate micropores and displace simulated oil, thereby enhancing the mobilization degree.

3.7. Oil migration mechanism analysis

In the initial stage of imbibition, the magnetic nanofluid contacts the oil phase and the core sample matrix. The magnetic nanoparticles migrate to the oil–water interface and solid–liquid interface through diffusion and convection, which reduces the interfacial tension, enhances the hydrophilicity of the core sample surface, and lowers the adhesion work required for oil detachment from the core sample surface (Lu and Wang, 2023). Under the influence of capillary forces, the magnetic nanofluid continues to enter the core sample. As the magnetic nanofluid further penetrates into the pore space through the throats, the interfacial energy increases, causing oil to be displaced from the core sample.

During the imbibition process, capillary force is the primary driving force, and it increases with decreasing pore diameter. Therefore, the magnetic nanofluid is first drawn into micropores, and the oil stored in these micropores is then displaced into mesopores and macropores. As the magnetic nanofluid continues to penetrate deeper into the core sample, the oil displacement in the micropores and mesopores approaches equilibrium, with the largest contribution to oil displacement coming from the macropores. Due to the heterogeneity and connectivity of the pores, the magnetic nanofluid enters through the micropores while oil is displaced from the macropores. In the final stage of imbibition, when the magnetic nanofluid has fully entered the pores, the effect of capillary force on oil displacement decreases, making it difficult for the remaining oil to be displaced, leading to the formation of residual oil.

3.8. Prospects

The application of nanomaterials is considered an indispensable pathway for future enhanced oil recovery. Owing to their small particle size and large specific surface area, nanomaterials can penetrate porous media and effectively adsorb at interfaces, thereby improving interfacial properties. The magnetic nanofluid developed in this work exhibits interfacial activity, strong wettability alteration capability, and excellent thermal and saline resistance. In addition, it can be magnetically recycled and reused, substantially reducing operational costs. These advantages endow it with great application potential, particularly for field implementation in low-permeability and ultra-low-permeability reservoirs as well as high-temperature and high-salinity reservoirs.

Nevertheless, it should be noted that due to the nanoscale size of the Fe_3O_4–TiO_2, achieving complete recycle during the current magnetic separation process is challenging. The recyclability experiment presented in this work therefore serves only as a preliminary demonstration of the recycle potential of the magnetic nanofluid rather than a comprehensive evaluation. Future research will focus on optimizing surface modifications of the nanoparticles to meet the performance requirements of specific reservoir conditions, while simultaneously improving magnetic separation methods, such as high-gradient magnetic separation or magnetic filtration, to enhance nanoparticle recycle efficiency and strengthen the practical applicability of the technology in field operations.

4. Conclusions

In this work, magnetic core–shell structured nanoparticles, Fe_3O_4–TiO_2, were synthesized using inexpensive and readily available Fe_3O_4 nanoparticles and tetrabutyl titanate as base materials. The magnetic nanofluid exhibited significant interfacial activity, excellent wettability alteration capacity, and superior temperature and salt resistance. At 80 °C, the spontaneous imbibition recovery of the magnetic nanofluid reached 32.19%, which is 3.59% higher than that of SiO_2 nanofluid. Moreover, the magnetic nanofluid demonstrated a recycle rate of 81.31% using a magnet, significantly reducing operational costs. Nuclear magnetic resonance experiments revealed that the final imbibition depth of the magnetic nanofluid was 18.82 mm, representing an increase of 21.97% compared with the SiO_2 nanofluid and 39.10% compared with the simulated formation water. The imbibition process of the magnetic nanofluid was governed by capillary forces, with the fluid first entering micropores and displacing the oil into macropores. This study can provide theoretical insights and technical support for the efficient development of low-permeability reservoirs.

CRediT authorship contribution statement

Zhen-Feng Ma: Writing – original draft, Methodology, Investigation. **Ming-Wei Zhao:** Writing – review & editing, Supervision, Funding acquisition. **Xiang-Yu Wang:** Methodology, Investigation. **Kai-Wen Liu:** Methodology, Investigation. **Yu-Xin Xie:** Data curation. **Yi-Zheng Zhang:** Data curation. **Zhong-Zheng Xu:** Visualization. **Cai-Li Dai:** Writing – review & editing, Resources, Funding acquisition.

Declaration of competing interest

The authors declare that they have no known competing financial interests or personal relationships that could have appeared to influence the work reported in this paper.

Acknowledgements

The work was supported by the National Natural Science Foundation of China (U24B2033, 52222403), Key Research and Development Program of Shandong Province (2022CXPT001), Taishan Scholar Program (tspd20230605, tsqn202211079), Shandong Energy Institute (SEI U202309), State Key Laboratory of Deep Oil and Gas (SKLDOG2024-ZYTS-15), and the Innovation Fund Project for Graduate Student of China University of Petroleum (East China) supported by “the Fundamental Research Funds for the Central Universities” (25CX04006A).

References

Behzadnia, A., Montazer, M., Rashidi, A., et al., 2014. Sonosynthesis of nano TiO_2 on wool using titanium isopropoxide or butoxide in acidic media producing multifunctional fabric. Ultrason. Sonochem. 21 (5), 1815–1826. https://doi.org/10.1016/j.ultsonch.2014.03.009.

Betancur, S., Carrasco-Marín, F., Pérez-Cadenas, A.F., et al., 2019. Effect of magnetic iron core–carbon shell nanoparticles in chemical enhanced oil recovery for ultralow interfacial tension region. Energy & Fuels 33 (5), 4158–4168. https://doi.org/10.1021/acs.energyfuels.9b00426.

Cao, M.J., Wang, R.Y., Li, Y.C., et al., 2024. Nanoparticle-enhanced water-based-emulsion fracturing fluid for improved imbibition recovery in unconventional reservoirs: Performance and mechanism. SPE J. 29 (7), 3732–3747. https://doi.org/10.2118/219739-PA.

Caselli, L., Traini, T., Micciulla, S., et al., 2024. Antimicrobial peptide coating of TiO_2 nanoparticles for boosted antimicrobial effects. Adv. Funct. Mater. 34 (39), 2405047. https://doi.org/10.1002/adfm.202405047.

Chen, Z., Su, Y.L., Li, L., et al., 2022. Characteristics and mechanisms of supercritical CO_2 flooding under different factors in low-permeability reservoirs. Pet. Sci. 19 (3), 1174–1184. https://doi.org/10.1016/j.petsci.2022.01.016.

Dembek, M., Bocian, S., Buszewski, B., 2022. Solvent influence on zeta potential of stationary phase–mobile phase interface. Molecules 27 (3), 968–978. https://doi.org/10.3390/molecules27030968.

Elkhatib, O., Youssif, M.I., Piri, M., et al., 2024. Mechanistic investigation of wettability alteration by bulk and interfacial asphaltenes using a surface force apparatus. Energy & Fuels 38 (1), 171–183. https://doi.org/10.1021/acs.energyfuels.3c04029.

Esfandiarian, A., Maghsoudian, A., Davarpanah, A., et al., 2022. Developing a novel procedure in utilizing pendant drop method for determination of ultra-low interfacial tension and surface tension in near-miscibility conditions. J. Petrol. Sci. Eng. 215, 110607. https://doi.org/10.1016/j.petrol.2022.110607.

Gholinezhad, S., Kantzas, A., Bryant, S.L., 2022. 1D magnetic resonance imaging and low-field nuclear magnetic resonance relaxometry of water-based silica nanofluids. Colloids Surf. A Physicochem. Eng. Asp. 640, 128480. https://doi.org/10.1016/j.colsurfa.2022.128480.

Kang, W.L., Zhou, B.B., Issakhov, M., et al., 2022. Advances in enhanced oil recovery technologies for low permeability reservoirs. Pet. Sci. 19 (4), 1622–1640. https://doi.org/10.1016/j.petsci.2022.06.010.

Kosmulski, M., Mączka, E., 2022. Zeta potential in dispersions of titania nanoparticles in moderately polar solvents stabilized with anionic surfactants. J. Mol. Liq. 355, 118972. https://doi.org/10.1016/j.molliq.2022.118972.

Li, H.Q., Wang, Y.Z., He, X.Y., et al., 2021. A green deep eutectic solvent modified magnetic titanium dioxide nanoparticles for the solid-phase extraction of chymotrypsin. Talanta 230, 122341. https://doi.org/10.1016/j.talanta.2021.122341.

Li, J.C., Zhang, S., Wang, L.L., et al., 2023. In situ growth of Fe_3O_4 nanoparticles in poly(arylene ether nitrile)/graphene/carbon nanotube foams for electromagnetic interference shielding. ACS Appl. Nano Mater. 6 (9), 7802–7813. https://doi.org/10.1021/acsanm.3c00925.

Li, N., Ke, H., Wang, T.Y., et al., 2022. Recyclable surface-functionalized Fe_3O_4 particles for heavy oil viscosity reduction. J. Petrol. Sci. Eng. 211, 110112. https://doi.org/10.1016/j.petrol.2022.110112.

Li, Y.M., Altalbawy, F.M.A., Rachchh, N., et al., 2025. Mitigating fines migration in low salinity water flooding of clay rich sandstones using TiO_2 Saponin Zr nanocomposites. Sci. Rep. 15 (1), 18870–18882. https://doi.org/10.1038/s41598-025-03348-2.

Liu, C., You, Q., Wang, T.R., et al., 2024. Study of microscopic imbibition and formation plugging mechanism of the compact oil reservoir based on SEM and NMR analysis. Fuel 357, 129672. https://doi.org/10.1016/j.fuel.2023.129672.

Liu, J.R., Sheng, J.J., 2020. Investigation of countercurrent imbibition in oil-wet tight cores using NMR technology. SPE J. 25 (5), 2601–2614. https://doi.org/10.2118/201099-PA.

Liu, Q., Li, J.L., Liang, B., et al., 2023. Complex wettability behavior triggering mechanism on imbibition: A model construction and comparative study based on analysis at multiple scales. Energy 275, 127434. https://doi.org/10.1016/j.energy.2023.127434.

Liu, Q., Zhang, Y.S., Zhao, X.S., et al., 2022. Enhanced oil recovery by foam flooding using foam stabilized with modified Fe_3O_4 nanoparticles. J. Petrol. Sci. Eng. 209, 109850. https://doi.org/10.1016/j.petrol.2021.109850.

Lu, X.K., Wang, M.R., 2023. Shape and surface property effects on displacement enhancement by nanoparticles. Int. J. Mech. Sci. 255, 108471. https://doi.org/10.1016/j.ijmecsci.2023.108471.

Mahdaviara, M., Sharifi, M., Ahmadi, M., 2022. Toward evaluation and screening of the enhanced oil recovery scenarios for low permeability reservoirs using statistical and machine learning techniques. Fuel 325, 124795. https://doi.org/10.1016/j.fuel.2022.124795.

Meng, L.M., Dai, Y.J., Zhao, M.W., et al., 2024. Investigation of carbon-based nanofluid imbibition processes in low-permeability reservoirs using nuclear magnetic resonance. Colloids Surf. A Physicochem. Eng. Asp. 695, 134310. https://doi.org/10.1016/j.colsurfa.2024.134310.

Nguyen, M.D., Deng, L.Z., Lee, J.M., et al., 2024. Magnetic tunability via control of crystallinity and size in polycrystalline iron oxide nanoparticles. Small 20 (43), e2402940. https://doi.org/10.1002/smll.202402940.

Noruzi, Y., Sharifi, M., Fahimpour, J., et al., 2024. The state-of-the-art of wettability alteration in sandstones and carbonates: A mechanistic review. Fuel 356, 129570. https://doi.org/10.1016/j.fuel.2023.129570.

Paryoto, S., Romdoni, Y., Kurnia, I., et al., 2023. Synergy of surfactant mixtures and Fe_3O_4 nanoparticles for Enhanced oil recovery (EOR). Inorg. Chem. Commun. 155, 111125. https://doi.org/10.1016/j.inoche.2023.111125.

Pereira, M.L.O., Maia, K.C.B., Silva, W.C., et al., 2020. Fe_3O_4 nanoparticles as surfactant carriers for enhanced oil recovery and scale prevention. ACS Appl. Nano Mater. 3 (6), 5762–5772. https://doi.org/10.1021/acsanm.0c00939.

Rouhani, M., Ashrafi, S.D., Taghavi, K., et al., 2022. Evaluation of tetracycline removal by adsorption method using magnetic iron oxide nanoparticles (Fe_3O_4) and clinoptilolite from aqueous solutions. J. Mol. Liq. 356, 119040. https://doi.org/10.1016/j.molliq.2022.119040.

Song, S.S., Li, C.J., Jia, W.L., et al., 2025. Adsorption behavior of asphaltene aggregates generated by self-association at the oil/water interface. Fuel 380, 133143. https://doi.org/10.1016/j.fuel.2024.133143.

Tavakkoli, O., Kamyab, H., Shariati, M., et al., 2022. Effect of nanoparticles on the performance of polymer/surfactant flooding for enhanced oil recovery: A review. Fuel 312, 122867. https://doi.org/10.1016/j.fuel.2021.122867.

Tohidi, Z., Teimouri, A., Jafari, A., et al., 2022. Application of Janus nanoparticles in enhanced oil recovery processes: Current status and future opportunities. J. Petrol. Sci. Eng. 208, 109602. https://doi.org/10.1016/j.petrol.2021.109602.

Valiei, A., Lin, N., McKay, G., et al., 2022. Surface wettability is a key feature in the mechano-bactericidal activity of nanopillars. ACS Appl. Mater. Interfaces 14 (24), 27564–27574. https://doi.org/10.1021/acsami.2c03258.

Wang, F.Y., Zeng, F.C., Wang, L., et al., 2023a. Experimental study of surfactant-aided dynamic spontaneous imbibition in tight oil reservoirs: The effect of fluid flow, displacement pressure, temperature, and fracture. Energy & Fuels 37 (23), 18632–18641. https://doi.org/10.1021/acs.energyfuels.3c03262.

Wang, X.Z., Peng, X.L., Zhang, S.J., et al., 2018. Characteristics of oil distributions in forced and spontaneous imbibition of tight oil reservoir. Fuel 224, 280–288. https://doi.org/10.1016/j.fuel.2018.03.104.

Wang, X.Y., Zhao, M.W., Wang, X.H., et al., 2023b. Synergistic effect of dual hydrogen-donor deep eutectic solvent for performance improvement of fracturing-oil expulsion fluids. Chem. Eng. J. 468, 143728. https://doi.org/10.1016/j.cej.2023.143728.

Wang, Y.Y., Yang, S.K., Zhang, J.W., et al., 2023c. Scalable and switchable CO_2-responsive membranes with high wettability for separation of various oil/water systems. Nat. Commun. 14 (1), 1108–1117. https://doi.org/10.1038/s41467-023-36685-9.

Wu, H.R., Chang, J.W., Xu, G.R., et al., 2024. In-situ emulsification and viscosification system of surfactant-assisted Janus nanofluid and its profile control effect. Advances. Geo-Energy Res. 14 (2), 135–146. https://doi.org/10.46690/ager.2024.11.06.

Xie, K., Wu, Z.Q., Liu, C.L., et al., 2024. A review of mechanisms and ML-based research on factors affecting spontaneous imbibition of surfactant. Geo-energy Sci. Eng. 240, 213071. https://doi.org/10.1016/j.geoen.2024.213071.

Xie, L.L., You, Q., Wang, E.Z., et al., 2022. Quantitative characterization of pore size and structural features in ultra-low permeability reservoirs based on X-ray computed tomography. J. Petrol. Sci. Eng. 208, 109733. https://doi.org/10.1016/j.petrol.2021.109733.

Yan, X., Dai, C.L., Wang, R.Y., et al., 2024. Experimental study on countercurrent imbibition in tight oil reservoirs using nuclear magnetic resonance and AFM: Influence of liquid–liquid/solid interface characteristics. Fuel 358, 130026. https://doi.org/10.1016/j.fuel.2023.130026.

Zarandona, I., Correia, D.M., Moreira, J., et al., 2023. Magnetically responsive chitosan-pectin films incorporating Fe_3O_4 nanoparticles with enhanced antimicrobial activity. Int. J. Biol. Macromol. 227, 1070–1077. https://doi.org/10.1016/j.ijbiomac.2022.11.286.

Zhang, T.T., Li, Z.P., Adenutsi, C.D., et al., 2022. Quantitative investigation of nanofluid imbibition in tight oil reservoirs based on NMR technique. Pet. Sci. 19 (5), 2185–2198. https://doi.org/10.1016/j.petsci.2022.04.013.

Zhao, M.W., Zhang, Y.M., Wu, W., et al., 2023. Role of ultralow interfacial tension in the imbibition of silica nanofluids. Energy & Fuels 37 (17), 12879–12888. https://doi.org/10.1021/acs.energyfuels.3c02303.

Zhao, M.W., Ma, Z.F., Song, X.G., et al., 2024. Study on the main factors and mechanism of functional silica nanofluid spontaneous imbibition for enhanced oil recovery. J. Mol. Liq. 394, 123699. https://doi.org/10.1016/j.molliq.2023.123699.